EurJIC
European Journal of Inorganic Chemistry

Full Papers
doi.org/10.1002/ejic.202000838

Chemistry Europe
European Chemical Societies Publishing

Preparation and Capacitance Properties of Graphene Quantum Dot/NiFe–Layered Double-Hydroxide Nanocomposite

Sara Samuei,*[a] Zolfaghar Rezvani,[b] Ashkan Shomali,[c] Emine Ülker,[d] and Ferdi Karadaş[e]

A new composite from graphene quantum dots (GQDs) and NiFe layered double hydroxide was successfully prepared by the coprecipitation method under optimal conditions. The nanoparticles of the composite were analyzed by X-ray diffraction (PXRD), Fourier transform infrared spectroscopy (FT-IR), scanning electron microscopy (SEM), and thermal gravimetric analysis (TGA) to obtain the structure, composition and morphology information. Also, the electrochemical properties were investigated by cyclic voltammetry, galvanostatic charge/discharge measurements, and electrochemical impedance spectroscopy. The nanocomposite displays a specific capacitance of 712.7 $F g^{-1}$ and excellent cycle life after 2500 cycles by applying 10 $A g^{-1}$ of the current density in 1 M KOH electrolyte, which confirms that the nanocomposite has superb capacitance retention (~94.8%) and can be used as a capable supercapacitor. Furthermore, this study provides a desirable procedure for the preparation of novel nanocomposites based on graphene quantum dots, which can be used in energy storage/conversion devices.

Introduction

Recently by increasing the energy crisis in the world and the rapid depletion of various fossil fuels, supercapacitors as energy storage tools have attracted much attention. These storage devices have a high capability and power density, a higher rate of charging/discharging, and a long life cycle [1–4]. Supercapacitors (SCs), which are also called electrochemical capacitors or ultracapacitors, can fall into these categories: Electrical double-layer capacitors (EDLCs) and pseudocapacitors [5–7]. The performance mechanism of electrochemical double-layer capacitors is relying on the charge separation between the electrode and electrolyte interfaces [8]. Mostly fabricated by carbon materials with the high surface area such as activated carbon, CNTs, carbon nanofibers, and graphene sheets that can be used in aqueous and non-aqueous solutions as electrolytes [9]. Nevertheless, because of the low energy densities of this kind of supercapacitors, their vast application has been limited [10]. While, pseudocapacitors electrodes mainly consist of transition metal oxides in several oxidation states, for instance, MnO_2 [11], RuO_2 [12], Co_3O_4 [13], $Ni(OH)_2$ [14], NiO [15]. These kinds of materials have higher capacitance because of the redox reactions between the surface and bulk part of transition metal oxides. The other category of materials used for pseudocapacitors electrodes is conducting polymers such as polyaniline, polypyrrole, and polythiophene. According to their mechanism, faradic charges transfer occurs between electrolyte (aqueous solutions) and electrode [1,16]., then the capacitance of pseudocapacitors is higher [17]. Up to now, a great deal of research has been done on the various electrode materials to improve the performance of supercapacitors. Among different transition metal hydroxides [18], Layered double hydroxides (LDHs), as some sort of 2D structure anionic clays, have appealed widespread consideration. Nontoxicity, low cost, high stability, excellent reversibility, and high specific capacitance have provided them to be great candidates for supercapacitor materials [19,20].

Layered Double Hydroxides (LDHs) are presented as anionic hydrotalcite-like clays with the typical chemical formula: $[M^{2+}_{1-x}M^{3+}_{x}(OH)_2]^{x+}(A^{n-})_{x/n}\cdot mH_2O$, where M^{2+} and M^{3+} are defined as di- and trivalent cations and A^{n-} is a variable anion respectively. X clarified as the ratio of $M^{3+}/(M^{2+}+M^{3+})$. The total charge of the layers depends on the ratio of M^{2+}/M^{3+} [21–23]. LDHs formed from transition metals contain abundant valence states that can provide excellent redox activity and acceptable cycling stability [24–26]. Previously, many studies tried to investigate the efficiency of LDHs as an electrode material for supercapacitors such as NiCo–LDH [27], NiCoAl–LDH [28], CoAl–LDH [29], NiMn–LDH [30] in basic electrolytes. However, because of having poor electric conductivity and low power performance,

[a] Dr. S. Samuei
Inorganic Chemistry Laboratory, Department of Chemistry, Faculty of Sciences, Azarbaijan Shahid Madani University,
East Azarbaijan, 5173865955 Tabriz, Iran
E-mail: SaraSamuei1411@gmail.com
https://scholar.google.com.tr/citations?user=e8YbRNIAAAAJ&hl=en
[b] Prof. Z. Rezvani
Inorganic Chemistry Laboratory, Department of Chemistry, Faculty of Sciences, Azarbaijan Shahid Madani University,
Tabriz, Iran
[c] Dr. A. Shomali
Department of Chemistry, Faculty of Sciences, Azerbaijan Shahid Madani University,
Tabriz, Iran
[d] Asst. Prof. E. Ülker
Department of Chemistry, Faculty of Arts & Science, Recep Tayyip Erdogan University,
Turkey
[e] Prof. F. Karadaş
Department of Chemistry, Bilkent University,
Turkey

their practical applications have been limited [31] to overcome these deficiencies preparing carbon-based nanocomposite can be used as a solution way [32]. For improving the conductivity in some studies, carbonaceous substances like carbon nanotubes, graphene, porous carbon, and carbon fibers have been applied [33]. For example, Wang et al. prepared the NiAl–LDH/graphene composites, which represents a specific capacitance of 781 $F g^{-1}$ while the pure NiAl–LDH has 566 $F g^{-1}$ specific capacitance [16]. Also, Zheng et al. investigate that CoAl–LDH/graphene composite has more capability compared to CoAl–LDH with a specific capacitance of 479 $F g^{-1}$ and 427 $F g^{-1}$, respectively [34]. One of the novel carbonaceous materials which have been a little-studied so far is graphene quantum dots (GQDs). GQDs exhibit excellent characteristics because of high surface area, abundant surface functional groups which provide a better surface connection with other parts of composite and the fast electron transfer through π-π conjunction; this leads the increases in the catalytic activity of the composites [35].

However, to date, no studies have been performed on the GQDs/NiFeLDH composite as electrode material for supercapacitors. In the current research work, preparation of the graphene quantum dot/Ni Fe–layered double hydroxide composite by a coprecipitation method has been done for the first time. The GQDs are prepared by pyrolyzing of the citric acid via a bottom-up approach [36], and also a solvent treatment for the separation process performed. Then nanocomposite of GQDs and NiFe–LDH is successfully synthesized by the coprecipitation procedure in the alkaline media. In this study, Fe^{3+} was chosen because compared to the other used ions such as cobalt and aluminum, iron is cheaper and more plentiful [37].

In order to obtain the compositional, morphological, and structural information, the prepared nanocomposite was analyzed by X-ray diffraction, Fourier transforms infrared spectroscopy, thermal gravimetric analysis, and scanning electron microscopy. The supercapacitor properties of the GQDs/NiFeAl–LDH composite as electrode examined by cyclic voltammetry (CV), galvanostatic charge/discharge, and finally, by electrochemical impedance spectroscopy (EIS).

Results and Discussion

XRD analyses

Figure 1 shows the XRD patterns of the resultant GQDs/NiFeAl–LDH composite compared with pristine NiFeAl–LDH (JCPDS Card 40-0215) and GQDs. The XRD pattern of the precursor graphene quantum dot (Figure 1a) represents a broad peak with a relatively low intensity near 27° belongs to the (002) plane. Figure 1b shows the XRD pattern of pure NiFe–LDH, the symmetric reflection of (003), (006), (110) related to the R3 m symmetry (a hexagonal lattice). Also, (113) planes and broad asymmetric peaks such as (009), (015), and (018) planes, belong to the hydrotalcite-like compounds [38]. For the GQDs/NiFe–LDHs composite, the diffraction peaks are similar to

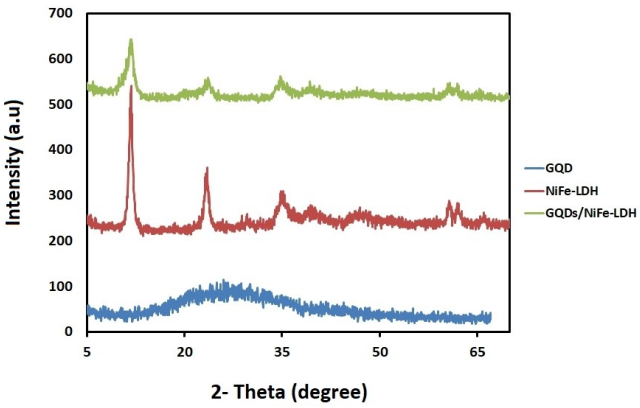

Figure 1. XRD patterns of GQDs, pristine NiFe–LDH, and GQDs/NiFe–LDH composite.

those of the pristine NiFe–LDHs. There is no shift in the location of the peaks, so it can be concluded that there is a similarity of the interlayer anions between the pristine NiFe–LDH and composite. Also, there are no other peaks in the spectrum, indicating a lack of impurities in the composite Just decreases in the intensity of the reflection peaks have occurred, which is associated with the disorder in the condensed structure of the composite compared to pure LDH [39].

FTIR Spectra

The FT-IR patterns of (a) GQDs, (b) pristine NiFe–LDH, and (c) GQDs/NiFeAl–LDH at ambient temperature are presented in Figure 2. spectrum 2a belongs to GQDs; As can be seen, there is a distinct peak located at approximately 1723 $cm^{-1,}$ which is specified to stretch of the carboxylic functional group (C=O), The broad peak of O–H is also set at 3550 cm^{-1}. In the case of NiFe–LDH, the stretching vibration of the metal–oxygen–metal is observed in the low-frequency area (below 1000 cm^{-1}) [40]. Vibration bands centered at 578.61 cm^{-1} and 436.50 cm^{-1} are

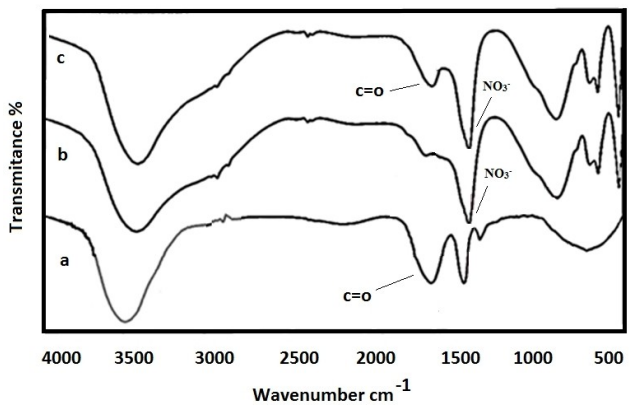

Figure 2. FT-IR spectrum of (a) GQDs, (b) pristine NiFe–LDH, and (c) the GQDs/NiFe–LDH composite.

showing the M–O–H and the O–M–O around respectively [41]. For spectrum b and c, the bands with peak maxima at 1384 cm^{-1} belongs to stretching modes of NO_3^- anions in the interlayer space and the robust broadband centered at 3480.91 cm^{-1} corresponds to hydroxyl groups stretching vibrations, which exists in the surface of LDH and interlayer water molecules [42]. Hydrogen bonds formed between interlayer water and hydroxyl groups cause the O–H peaks of LDHs, can be seen at low frequencies compared with free water [43]. By comparison of NiFe–LDH and pure graphene quantum dots, it can be observed that the spectrum pattern of composite has additional sharp peaks which are corresponded to characteristic signals of pure LDH and GQDs simultaneously. For example, carbonyl and nitrate peaks that confirm graphene quantum dots are not entered in the interlayer spaces. Though, they exist on the surface of LDH, which SEM analyses confirm this result.

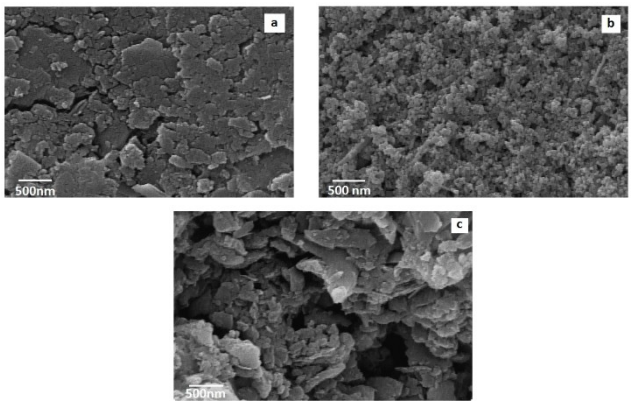

Figure 3. SEM micrographs of (a) pristine NiFe–LDH (b) GQDs, and (c) the GQDs/NiFe–LDH composite.

SEM analyses

SEM imaging was utilized to investigate the morphology of GQDs/NiFe–LDHs nanocomposite and its comparison with pristine LDH and GQDs (Figure 3), as can be seen in Figure 3a, the LDH includes unequal particles with rough surfaces that can conclude agglomeration had occurred. In NiFe–LDH due to partial replacement of Ni^{2+} by Fe^{3+}, the self-aggregation of double hydroxide layers had happened, and the electrostatic interaction between composing elements is enhanced, which leads to irregular denser nanosheets of the samples [44].

Figure 3b represents GQDs morphology, which shows spherical and homogeneous particles with dimensions below 50 nm approximately and has more pores than pure LDH. It is worth to note that the morphology of the composite Figure 3c is notably different from that of pristine LDHs and GQDs. In the SEM image of GQDs/NiFe–LDH composite, GQDs have covered the entire surface of LDHs, boost the surface area, and augment the more active sites and by increasing pores amount [37].

Figure 4a shows the TEM image of synthesized GQDs dispersed in ethanol. The GQDs observed are small and uniform,

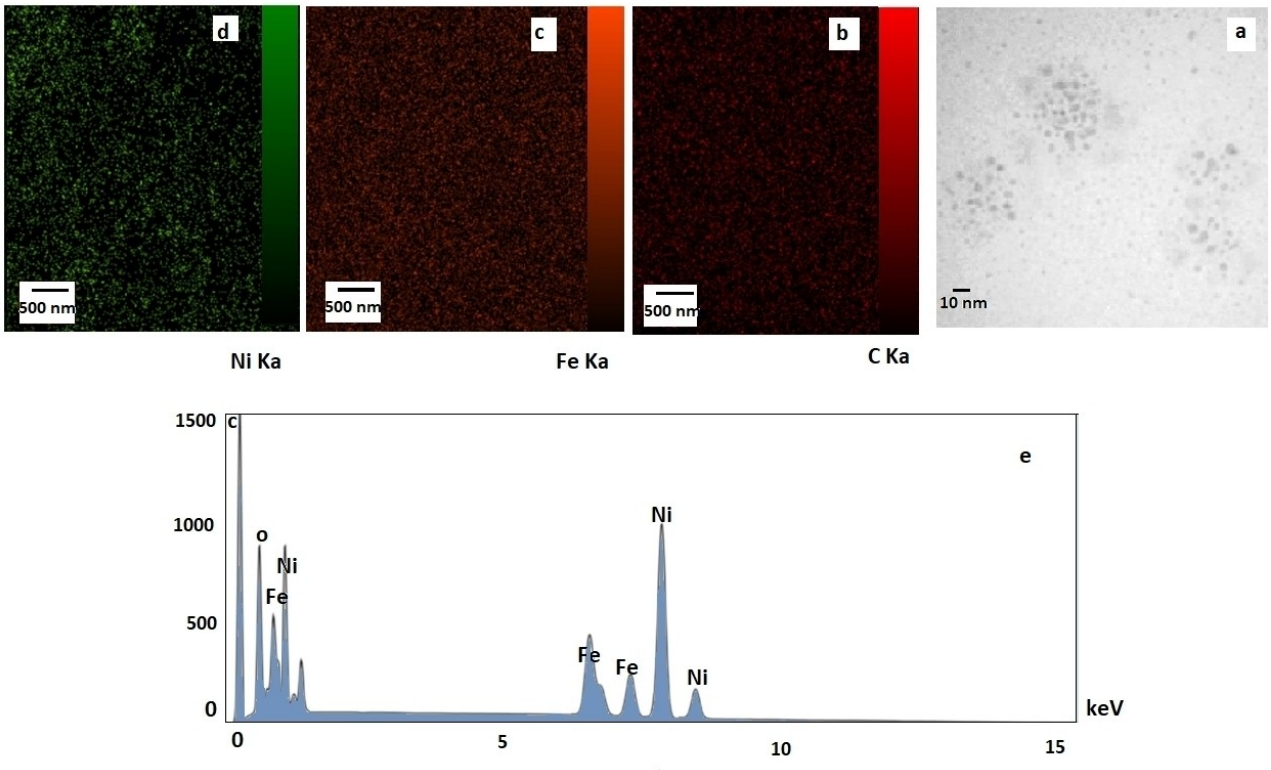

Figure 4. TEM image of GQDs (a), element maps showing the distribution of elements C(b), Fe (c), Ni (d), and EDX result of the GQDs/NiFe–LDH composite (e).

with an average diameter of 5 nm. Figure 4b, Figure 4c and d show the elemental mapping of the composite. The carbon element of GQDs uniformly distributed on the LDH surface and overlapped with Ni and Fe elements, which are the main constituents of LDH. Figure 4e displays the EDX spectrum of GQD/NiFe–LDH; the result confirms the presence of carbon and oxygen of GQDs with NiFe particles [45,46].

The zeta potential of synthesized GQDs is determined −25 mV due to the presence of abundant Oxygen contained functional groups on the surface, GQDs are negatively charged [47]. Table 1 shows Result of zeta potential, electrophoretic mobility, and conductivity of GQDs. Figure 5 also represents the particle size distribution of GQDs in ethanol. The average size of GQD nanoparticles is 6.65 ± 2.20 nm with high intensity which can be seen in the figure.

Thermogravimetry and differential thermal analysis

Thermogravimetric analysis (TGA) and differential thermal analysis (DTA) patterns for pure NiFe–LDH and GQDs/NiFe–LDH nanocomposite are illustrated in Figure 6. Figure 6a shows that the decomposition of NiFe–LDH has appeared in two steps. The first step is related to the release of water molecules from the LDH surface and interlayer space in the ranges between 100–180 °C. The second stage belongs to the dihydroxylation of octahedral layers in LDHs within the ranges of 250–350 °C. In the DTA, two peaks can be observed for pure LDH first peak belongs to the removal of water molecules at around 110 °C, and the second intense peak corresponds to dehydration of LDH layers around 280 °C. Figure 6b is for the GQDs/NiFe–LDH, in which there a remarkable shift to the high temperatures has occurred. The first and second step shifts are quite obvious, which observed at around 250 °C and 380 °C, respectively, and

Table 1. Zeta potential, electrophoretic mobility, and conductivity of CQDs.

Sample name	Zeta potential	Conductivity	Mobility	Field strength
GQD	−25.9 mV	120 uS/cm	2.60 u/s/V/cm	5.0 kV/m

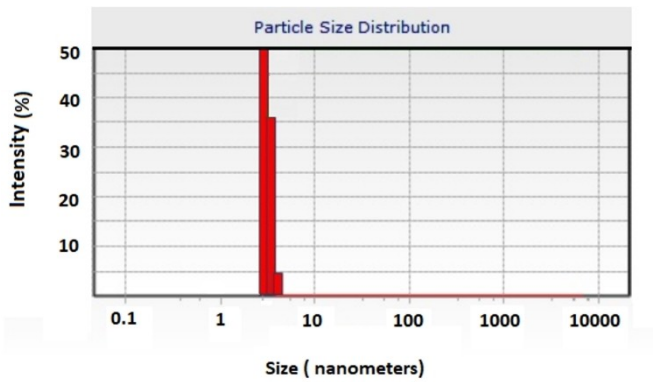

Figure 5. Particle size distribution of GQDs in ethanol.

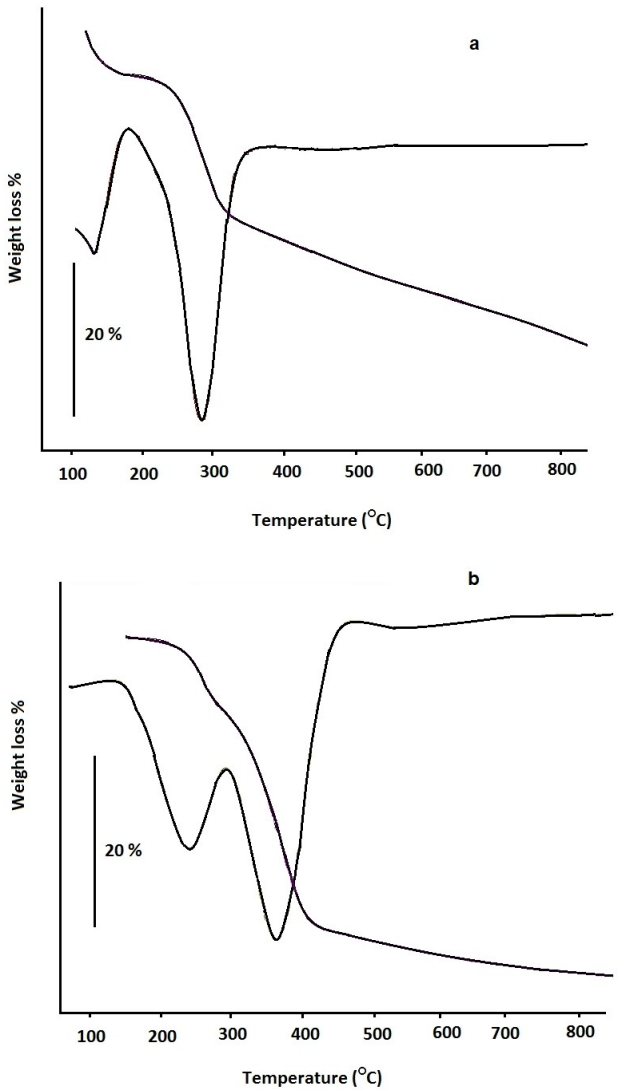

Figure 6. TGA pattern of (a) NiFe–LDH and (b) GQDs/NiFe–LDH nanocomposite.

confirm that thermal stability happened in the nanocomposite [48]. Thermal stability can occur because of synergetic effects between two parts of the nanocomposite. As reported in the literature, synergetic effects can improve the properties of each component. This result is corresponds to the presence of the strong interaction between functional groups of each material such as Coulombic electrostatic force and hydrogen bonds [49,50]. Also, GQDs participation leads to better linkage with the LDH matrix and less residual/unreacted functional groups in both LDH and GQDs [51].

Electrochemical studies

The electrochemical tests were used to explore the electrochemical performance of the nanocomposite. A three-electrode electrochemical system by the Cyclic Voltammetry (CV) method was used to evaluate the super capacitance performance of the

GQDs/NiFe–LDH, NiFe–LDH and, GQDs in 1 M KOH aqueous electrolyte in the scan rate of 20 mV s^{-1} (Figure 7). For this purpose, Ag/AgCl and platinum wire were applied as the reference electrode and the counter-electrode, respectively. The tests were done under similar conditions for evaluation. A pair of redox peaks can be seen in the curve of NiFe–LDH and GQDs/NiFe–LDH nanocomposite, which is related to Ni (III)/Ni(II) couple. A comparison of the electrochemical performance of the GQDs and NiFe–LDH, by the GQDs/NiFe–LDH electrodes, illustrated that the oxidation and reduction peak currents of the Ni (III)/Ni (II) couple for GQDs/NiFe–LDH enhance with the increase of base current by imbalance shape. Also, the distance of a peak to peak (between the anode and cathode peaks) for the nanocomposite modified electrode is less than for the other states. Besides, the Oxidation and reduction peaks of the Ni (III)/Ni(II) couple in the GQDs/NiFe–LDH electrode shifts to the negative potentials and displays high reversibility than the same couple in the pure LDH. Also, the GQDs/NiFe–LDH nanocomposite presented the largest integrated area, compared with the GQDs and NiFe–LDH, indicating that the GQDs/NiFe–LDH had the highest specific capacitance because of the increased surface area [52]. It can be clarified that the introduction of GQDs was efficiently prevented the accumulation of LDH and also hindered the loss of the active surface area of the composite. This result indicates that the nanocomposite charge transfer not only relies on the Redox mechanism but is also based on the synergistic effect. The presence of GQDs provides a considerable contribution between two parts of the composite, which can effectively increase the electrical conductivity of the composite. Also, GQDs cause better spreading of the electroactive sites and the surface area. As a result, the electron transfer in the nanocomposite electrode occurs more comfortable and faster than in the pure NiFe–LDH [53, 54]. For this reason, the base current of nanocomposite has increased with increasing scan rates and the Oxidation and reduction peaks of the Ni (III)/Ni(II) couple peaks will not be visible gradually.

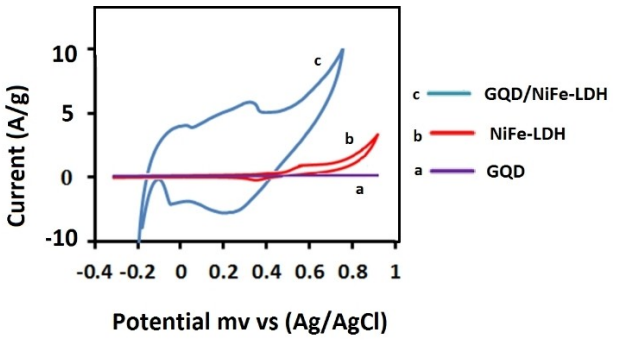

Figure 7. Cyclic voltammograms of (a) GQDs, (b) NiFe–LDH, and (c) GQDs/NiFe–LDH nanocomposite at a scan rate of 20 mV s^{-1} in 1 M KOH.

Figure 8a shows the CV curves of Ni–Fe LDH in the various scan rates. There is a direct relationship between increasing

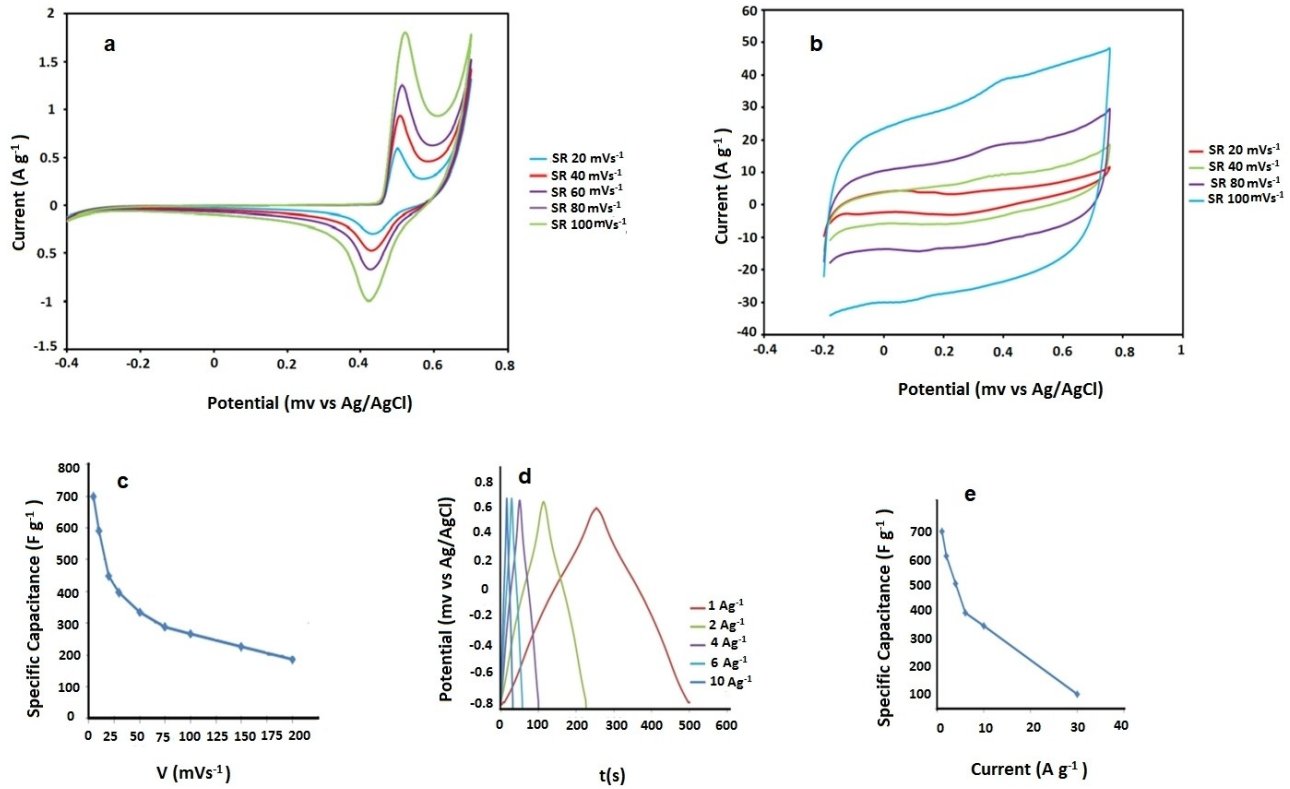

Figure 8. (a) CV curves of NiFe–LDH and (b) GQDs/NiFe–LDH electrode at different scan rates. (c) Variation of specific capacitance as a function of the scan rate for GQDs/NiFe–LDH nanocomposite. (d) Charge/discharge curves of GQDs/NiFe–LDH electrode at various current densities. (e) Variation of specific capacitance at various current densities.

scan rates and improving the current response of redox peaks, which depicts the pseudo-capacitive behavior of the LDH. Figure 8b represents CV curves of GQDs/Ni–Fe–LDH composite, which can be seen as current response enhanced by increasing scan rates. There are also apparent changes in the shape of the curves. This means the base current and the redox current of active material are enhanced at the same time by providing accelerating charge and electron transfer of the nanocomposite. ν represents the potential scan rates (mV s^{-1}). I (The current) defines as the current response (A. g^{-1}) concerning the mass of electroactive material under study. As shown in the figure, the CV curves of the GQDs/NiFe–LDH electrode from −0.2 to 0.7 V (vs. Ag/AgCl) at the scan rates of 20, 400, 80, and 100 mV s^{-1}, have been studied respectively. All CV curves have similar shapes; the quasi-rectangular curves in this study are due to the fast charge/discharge process characteristic, indicating the ideal capacitive behavior of double-layer capacitance. Figure 8c represents the change of the specific capacitance based on the scan rates for the GQDs/NiFe–LDH electrode. As depicted in the figure, the Cs of the electrode changes from 712.7 to 180 F g^{-1} with a scan rate from 10 to 200 mV s^{-1}. As a result, by comparing of the Cs at low scan rates, and high scan rates, it can be observed that by increasing the scan rate, a decline in the over-all Cs has occurred. At lower scan rates, electrolyte ions have enough time to enter the pores of the material, which leads to provides more accessible surface for redox reactions [55]. Galvanostatic charge/discharge electrochemical studies were performed to investigate the super capacity efficiency of the GQDs/NiFe–LDH electrode. Figure 8d represents the charge/discharge curves in the potential of −0.8 to 0.7 V for the GQDs/NiFe–LDH electrode in 1 M KOH solutions, at current densities ranging from 1 to 10 A g^{-1}, respectively. As shown in the figure, all of the curves are linear with the shape of triangular, sharp, and symmetric. It also has been explained that the ideal performance of the capacitor versus the time is dependent on the equal charging and discharging process, which specifies the reversible performance and high Coulombic proficiency. The longest charge/discharge time, implying the highest specific capacitance. That shows with the increase of the current density from 1 to 10 A g^{-1} charge/discharge time decreases. It can be concluded that there is a limitation in the transfer of alkaline ions of electrolyte to the electrode surface during the charge storage process, which causes the charge/discharge time decreases with increasing current density [56].

Figure 8e shows the performance rate of the GQDs/NiFe–LDH electrode based on various current densities. As can observe, the Cs of the GQDs/NiFe–LDH electrode declines with the rising current density. The Cs of the GQDs/NiFe–LDH electrode was obtained 712.7 F g^{-1} at the current density of 1 A g^{-1}. Table 2 shows materials that reported the literature for comparison purposes. As can be seen in Table 2, Many nanocomposites have been studied in energy conversion and storage applications, but research about developing highly efficient catalysts is still going on. GQDs have unique properties such as more abundant active sites (edges, functional groups, dopants, etc.), large surface area, solubility, and the ability to facilitate charge transfer.

Additionally, they can easily form composites with other nanomaterials. This composite was prepared for the first time. Unlike the other Nano carbonic materials, GQDs used for this research were prepared by the simple one-pot method without needing to age in high temperatures or a long time, just in 30 minutes. Also, there is no need to use strong acid-base treatment for purification. In addition to the ease and cost-effectiveness of the preparation method, it is worth to not that It is classified between the efficient capacitor materials because of the excellent cycle life after 2500 cycles and high specific capacitance [66–69].

For the investigation of charge storage capacity during the time, The CCV technique can be applied as the best tool [70, 71]. In this method, the stability of the electrodes evaluated under a long period of potential. The calculated Cs are considered being a function of the cycle numbers presented in Figure 9. As can be seen, The Cs value based on cycle numbers decreases slightly. As a result, after 2500 cycles, at the scan rate of 200 mV s^{-1}, 94.8 % of SC value preserved.

This result confirms that GQDs/NiFe–LDH electrode is highly stable during potential cycling tests [72].

Additionally, the EIS is used as a suitable method to evaluate the performance of supercapacitor and impedance of electrode materials. EIS was applied to determine the charge transfer property of materials and diffusion properties of ions [73]. The slope of the curve at low frequencies illustrates the diffusion of ions in the electrolyte over the electrode surface. Figure 10 demonstrates the Nyquist impedance plot (imaginary part, Z′, versus real factor, Z″) over the frequency range 0.01–100 kHz, for the NiFe–LDH (a) and GQDs/NiFe–LDH electrodes (b) in 1 M KOH solution, at the potential of 0.4 V (about the

Table 2. Comparison of the specific capacitance and cycle retention.

Nanocompositematerials	Cs	Cycle retention	References
MgFe–hydrotalcite/polyaniline	593(2 A g^{-1})	87.0 % (500 Cycles)	[57]
NiCo2O4@NiFe–LDH	12.3 (F Cm^{-2})	83.1 % (1000 Cycles)	[58]
MnOOH/NiAl–LDH	1331.11 (F g^{-1})	82.4 % (1000 Cycles)	[59]
RGO/NiCo–LDH	2130(2 A g^{-1})	72.7 % (10000 Cycles)	[60]
RGO/CoAl–LDH	1492(F g^{-1})	94.3 % (5000 Cycles)	[61]
NiV–LDH	1581(F g^{-1})	79 % (2000 Cycles)	[62]
N-doped RGO/Ni–Co–LDH	1720(3 A g^{-1})	83 % (10000 Cycles)	[63]
NiMn–LDH	1881(F g^{-1})	79 % (2000 Cycles)	[64]
CoAl–LDH/graphene	479 (F g^{-1})	75 % (5000 Cycles)	[34]
NiO/NiMn–LDH	937 (F g^{-1})	91 % (1000 Cycles)	[65]

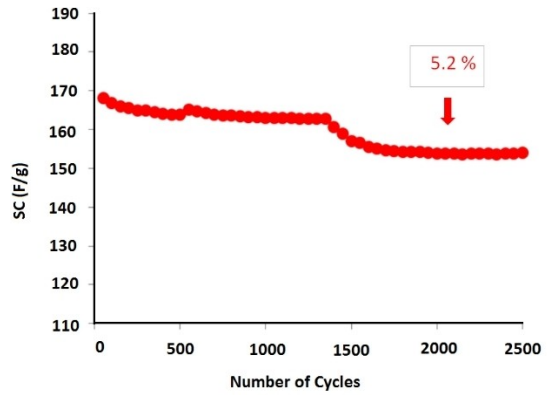

Figure 9. Retention of the Specific Capacitance of the GQDs/NiFe–LDH electrode as a function of the number of cycles at 2500 mV s^{-1}.

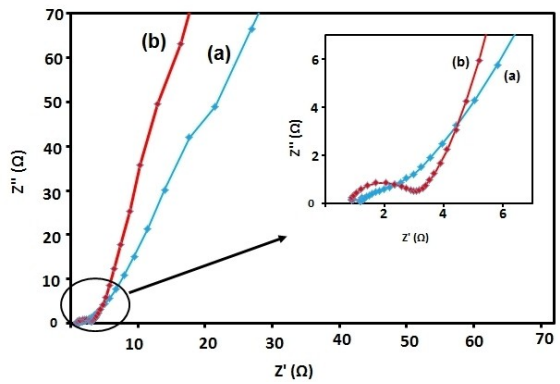

Figure 10. Nyquist plots of (a) NiFe–LDH electrode and (b) GQDs/NiFe–LDH electrode in the frequency range from 0.01 Hz to 100 kHz.

highest current of the cyclic voltammetry range). The inset of Figure 10 also compares the Nyquist plots of two electrodes by magnification in the higher frequencies. The EIS curve shows semicircle behavior at higher frequencies and linear behavior in the lower frequencies. The semicircle behavior indicates the presence of a Faradaic charge transfer resistance (R_{ct}). This is correlated to the reaction of the electric double-layer capacitor on the surface of the electrode. As seen in Figure 10, GQDs/NiFe–LDH electrode (a) displays a higher charge transfer resistance than the NiFe–LDH electrode (b), so as expected, the R_{ct} of nanocomposite is higher than the individual LDH. As can be detected, the width of the semicircle diameter for GQDs/NiFeLDH is about 2 Ω. In the lower frequencies, the Warburg tail, which appears at about 45°, is related to the capacitor's diffusive resistance of the electrolyte in the electrode pores and the ion dispersion in the electrode surface. The more the Nyquist plot gets closer to vertical, the more the electrochemical behavior of the electrode, similar to an ideal capacitor [74]. The vast Warburg region (the straight line) of the electrode represents the significant changes in ion diffusion, due to the enhancement of the obstruction in the movement of ions [54, 75]. It is also worth mentioning that the electrode at the higher frequencies represents series resistance (Rs) in the electrode/electrolyte system, which is related to the electrolyte and electronic resistance of the electrode simultaneously. In other words, the difficulty of solution conductivity is determined by Rs value. The Rs of the electrode was achieved from the intersection point of the Nyquist plot for (a) NiFe–LDH electrode, and (b) GQDs/NiFe–LDH electrode is 1.2 Ω and 1 Ω, respectively. These impressive electrochemical properties of nanocomposite can be due to the following reasons: The GQDs/NiFe–LDH structure can provide excess and available active sites, which make the diffusion distance, reduced, and enhance the kinetics of mass transfer. Additionally, increased porosity affects not only the ionic mobility of electrolyte but also keeps more electrolyte molecules in touch with pores during the reversible charging-discharging process.

Conclusion

In summary, we reported the synthesis of novel nanocomposite derived by GQDs and NiFe–LDH. The electrochemical properties of the nanocomposite have been investigated to study the possibility of using this material in the super capacitance application. GQDs/NiFe–LDH electrode exhibits remarkable electrochemical activity, including impressive specific capacity, high rate capability, and excellent cycling stability. Due to the enhancement of the surface area and pore amounts, a vast number of channels was formed that can provide maximum contact area between compounds and the electrolyte. Also, the synergetic effect between GQDs and NiFe–LDH provides higher conductivity and accelerates the diffusion of ions in the electrode surface in the charge/discharge process. The specific capacitance of GQDs/NiFe–LDH is 712.7 F g^{-1} at a current density of 1 A g^{-1} with an excellent cycling lifespan (~94.8% capacitance retention after 2500 cycles) determined. It can be concluded that GQDs/NiFe–LDH can be an ideal candidate for application in supercapacitors.

Experimental Section

Materials

All the required materials such as Ni $(NO_3)_2 \cdot 6H_2O$ and Fe $(NO_3)_3 \cdot 6H_2O$, NaOH, HCl are the Merck factory products and have an analytical grade of purity. All of the synthesis steps performed using double distilled water. The adjustment of pH was achieved by adding various amounts of 0.1 M solution of HCl and 0.1 M solutions of NaOH. Acetylene black and Polyvinylidene fluoride (PVDF) was purchased from Sigma and used without any purification.

Preparation of GQDs

The GQDs produced by pyrolyzing of the citric acid, as mentioned in the references [26] according to this procedure, 2 g citric acid, were placed into an autoclave, and the temperature reached to 180 °C. After half an hour of the pyrolysis process, citric acid molecules converted into carbon nanoparticles, which leads to the formation of pale yellow liquid. Increasing the temperature and

increasing the heating will change the color of the solution and yellow color, turning into an orange color, which indicates the formation of the graphene quantum dot has completed. For pH neutralization and bringing it to 7.0, 0.1 M NaOH slurry was added gradually into the obtained orange liquid under severe stirring [36]. When the pH setting finished, the solvent treatment and the separation process was done by the same amount of chloroform and distilled water. The aqueous orange solution contains GQDs preserved at 4 °C for investigation and further consumption.

Nanocomposite synthesis

The coprecipitation procedure was used to synthesize the GQDs/NiFe–LDH nanocomposite. Typically, Ni $(NO_3)_2 \cdot 6H_2O$ and Fe $(NO_3)_3 \cdot 6H_2O$ (Ni: Fe = 2:1) were prepared as a 30 ml aqueous solution and added gradually to 20 ml of the sonicated GQDs solution, with severe stirring. pH adjustment at 9.5 is made by adding a 2 M NaOH solution to the metal solutions. The reaction was done under the N_2 atmosphere, and the temperature of the solution was kept at 70 °C. The final solution was aged for 24 hours. After filtration of slurry by using a centrifuge, the resulted precipitation washed three times with double distilled water and dried completely at 60 °C.

Electrochemical measurements

The electrochemical tests were done as follows: The prepared nanocomposite was mixed with acetylene black and Polyvinylidene fluoride (PVDF) in a mass ratio of 85:15:5 and dispersed in N-methyl-2-pyrrolidinone (NMP) to form a homogeneous paste. Then the paste was compressed on to a piece of stainless steel as a current collector under a pressure of 10 MPa. Finally, the prepared electrode was dried at 80 °C for four h. The electrochemical tests were performed by using a three-electrode cell at ambient temperature. The stainless steel grid covered by electroactive materials was applied as the working electrode, a Pt foil with the area of 1 $cm^{2,}$ and an Ag/AgCl (saturated KCl) electrode were used as the counter and reference electrodes, respectively; 1 M KOH solution used as the electrolyte. A type of electrochemical workstation which used was Autolab PGSTAT 204. Through it, all the electrochemical investigations, including Cyclic voltammetry (CV), Galvanostatic charge/discharge (GCD), and electrochemical impedance spectroscopy (EIS) were done. The CV tests were obtained between −0.2 and 0.7 V (vs. Ag/AgCl) at various scan rates at the ranges of 10–200 mVs^{-1}. Galvanostatic charge/discharge (GCD) was recorded in the potential range of −0.8–0.7 mV at different current densities. EIS measurements were done by applying an AC voltage with 0.4 mV amplitude in the frequency range of 0.01 to 100 kHz.

The specific capacitance of a single electrode can be reckoned through the charge/discharge curve according to the following equation [76,77]:

$$Cs = \frac{\int I \times \Delta V}{\Delta V \times m\upsilon}$$

Where Cs (F/g) is specific capacitance, m (g) is the mass of the electroactive material coated on the electrode surface, I (A) is the response current, and ΔV (V) is the potential range, and υ (mVs^{-1}) is the scan rate, respectively. The lower the thickness of the electroactive material on the electrode surface, the less aggregation during the charge-discharge process happens. Additionally, The specific capacitance can be diminished with the increase of mass loading due to self-aggregation, which causes trouble in the electrolyte permeation and electron transfer [58,78].

Physicochemical characterization of the nanocomposite

An advanced diffractometer by the type of Bruker AXS (Germany) with the D8 model was used to record Powder X-ray diffraction (PXRD) spectra of the materials. Cu Ka radiation (l = 1.54 A°) at 40 kV and 35 mA with a Bragg angle ranging from 3 to 70 was applied. The Bruker (Germany) spectrophotometer was used for FTIR investigation in the range of 400–4000 cm^{-1} and KBr disk used at ambient temperature. Hana pH-meter model 211 was performed in the pH setting. Mettler Toledo TGA 851e device (Germany) recorded the thermogravimetric (TGA) curves with a heating rate of 10 °C min^{-1} under the N_2 atmosphere. Scanning electron microscopy (SEM; LEO 440i) at 20 keV was also used for the morphology investigation of the samples. The TEM images were obtained by a Zeiss EM10 C transmission electron microscope. Zeta potential data was obtained by Nanotrac Wave (Microtrac Company).

Acknowledgements

The authors are grateful for the support from Azarbaijan Shahid Madani University.

Conflict of Interest

The authors declare no conflict of interest.

Keywords: Graphene Quantum dots · Layered double hydroxides · Nanocomposites · Supercapacitors

[1] M. Winter, R. J. Brodd, ACS Publications.*Chem. Rev.* **2004**.
[2] M. D. Stoller, S. Park, Y. Zhu, J. An, R. S. Ruoff, *Nano Lett.* **2008**, *8*, 3498–3502.
[3] L. L. Zhang, X. S. Zhao, *Chem. Soc. Rev.* **2009**, *38*, 2520–2531.
[4] J. R. Miller, P. Simon, *Science.* **2008**, *321*, 651–652.
[5] B. E. Conway, *Springer Science & Business Media.* **2013**.
[6] J. Yan, Q. Wang, T. Wei, Z. Fan, *Adv. Energy Mater.* **2014**, *4*, 1300816.
[7] Y. Xiao, D. Su, X. Wang, S. Wu, L. Zhou, Z. Sun, Z. Wang, S. Fang, F. Li, *Electrochim. Acta.* **2017**, *253*, 324–332.
[8] X.-M. Liu, Y.-H. Zhang, X.-G. Zhang, S.-Y. Fu, *Electrochim. Acta.* **2004**, *49*, 3137–3141.
[9] J. Xu, S. Gai, F. He, N. Niu, P. Gao, Y. Chen, P. Yang, *Dalton Trans.* **2014**, *43*, 11667–11675.
[10] H. Pang, X. Li, B. Li, Y. Zhang, Q. Zhao, W.-Y. Lai, W. Huang, *Nanoscale.* **2016**, *8*, 11689–11697.
[11] D. Susanti, D.-S. Tsai, Y.-S. Huang, A. Korotcov, W.-H. Chung, *J. Phys. Chem. C.* **2007**, *111*, 9530–9537.
[12] V. Subramanian, H. Zhu, B. Wei, *J. Power Sources.* **2006**, *159*, 361–364.
[13] J. Xu, L. Gao, J. Cao, W. Wang, Z. Chen, *Electrochim. Acta.* **2010**, *56*, 732–736.
[14] B. Zhao, X.-K. Ke, J.-H. Bao, C.-L. Wang, L. Dong, Y.-W. Chen, H.-L. Chen, *J. Phys. Chem. C.* **2009**, *113*, 14440–14447.
[15] H. Wang, H. S. Casalongue, Y. Liang, H. Dai, *J. Am. Chem. Soc.* **2010**, *132*, 7472–7477.
[16] Z. Gao, J. Wang, Z. Li, W. Yang, B. Wang, M. Hou, Y. He, Q. Liu, T. Mann, P. Yang, *Chem. Mater.* **2011**, *23*, 3509–3516.
[17] J. Ji, L. L. Zhang, H. Ji, Y. Li, X. Zhao, X. Bai, X. Fan, F. Zhang, R. S. Ruoff, *ACS Nano.* **2013**, *7*, 6237–6243.
[18] X. Huang, Z. Zhang, H. Li, Y. Zhao, H. Wang, T. Ma, *J. Alloys Compd.* **2017**, *722*, 662–668.
[19] R. Patel, J. T. Park, M. Patel, J. K. Dash, E. B. Gowd, R. Karpoormath, A. Mishra, J. Kwak, J. H. Kim, *J. Mater. Chem. A.* **2018**, *6*, 12–29.
[20] S. Samuei, Z. Rezvani, A. R. Amani-Ghadim, *Environ. Prog. Sustain.* **2017**, *36*, 372–381.
[21] L. Ai, J. Jiang, *Eng. Sci.* **2012**, *192*, 156–163.

[22] H. Yan, W. Zhang, X. Kan, L. Dong, Z. Jiang, H. Li, H. Yang, R. Cheng, *Colloids Surf. A Physicochem. Eng. Asp.* **2011**, *380*, 143–151.
[23] S. Samuei, Z. Rezvani, B. Habibi, M. S. Oskoui, *Appl. Clay Sci.* **2019**, *169*, 31–39.
[24] A. D. Jagadale, G. Guan, X. Li, X. Du, X. Ma, X. Hao, A. Abudula, *J. Power Sources.* **2016**, *306*, 526–534.
[25] J. Han, H.-Y. Zeng, X. Cao, C.-R. Chen, *J. Mater. Sci. Mater. Electron.* **2017**, *28*, 2754–2762.
[26] S. Samuei, J. Fakkar, Z. Rezvani, A. Shomali, B. Habibi, *Anal. Biochem.* **2017**, *521*, 31–39.
[27] Y. Zhao, H. Ma, S. Huang, X. Zhang, M. Xia, Y. Tang, Z.-F. Ma, *ACS Appl. Mater. Interfaces.* **2016**, *8*, 22997–23005.
[28] V. Gupta, S. Gupta, N. Miura, *J. Power Sources.* **2009**, *189*, 1292–1295.
[29] Z. Lu, W. Zhu, X. Lei, G. R. Williams, D. O'Hare, Z. Chang, X. Sun, X. Duan, *Nanoscale.* **2012**, *4*, 3640–3643.
[30] X. L. Guo, J. M. Zhang, W. N. Xu, C. G. Hu, L. Sun, Y. X. Zhang, *J. Mater. Chem. A.* **2017**, *5*, 20579–20587.
[31] K. Qin, L. Wang, S. Wen, L. Diao, P. Liu, J. Li, L. Ma, C. Shi, C. Zhong, W. Hu, *J. Mater. Chem. A.* **2018**, *6*, 8109–8119.
[32] T. Yan, R. Li, Z. Li, *Mater. Res. Bull.* **2014**, *51*, 97–104.
[33] D. He, H. Tang, Z. Kou, M. Pan, X. Sun, J. Zhang, S. Mu, *Adv. Mater.* **2017**, *29*, 1601741.
[34] L. Zhang, K. N. Hui, K. San Hui, H. Lee, *Electrochim. Acta.* **2015**, *186*, 522–529.
[35] A. Muthurasu, S. S. Mers, V. Ganesh, *Int. J. Hydrogen Energy* **2018**, *43*, 4726–4737.
[36] Y. Dong, J. Shao, C. Chen, H. Li, R. Wang, Y. Chi, X. Lin, G. Chen, *Carbon.* **2012**, *50*, 4738–4743.
[37] M. Li, R. Jijie, A. Barras, P. Roussel, S. Szunerits, R. Boukherroub, *Electrochim. Acta.* **2019**, *302*, 1–9.
[38] Y. Guo, Z. Zhu, Y. Qiu, J. Zhao, *J. Hazard. Mater.* **2012**, *239*, 279–288.
[39] L. Li, R. Ma, Y. Ebina, K. Fukuda, K. Takada, T. Sasaki, *J. Am. Chem. Soc.* **2007**, *129*, 8000–8007.
[40] D. Kang, X. Yu, S. Tong, M. Ge, J. Zuo, C. Cao, W. Song, *Chem. Eng.* **2013**, *228*, 731–740.
[41] Y. Tian, G. Wang, F. Li, D. G. Evans, *Mater. Lett.* **2007**, *61*, 1662–1666.
[42] M. K. Titulaer, J. B. H. Jansen, J. W. Geus, *Clays Clay Miner.* **1994**, *42*, 249–258.
[43] M. Wei, X. Xu, J. He, Q. Yuan, G. Rao, D. G. Evans, M. Pu, L. Yang, *J. Phys. Chem. Solids.* **2006**, *67*, 1469–1476.
[44] W. Guo, C. Yu, S. Li, J. Yang, Z. Liu, C. Zhao, H. Huang, M. Zhang, X. Han, Y. Niu, *Small.* **2017**, *13*, 1701288.
[45] H. Chen, Z. Chen, G. Zhao, Z. Zhang, X. Wang, *J. Hazard. Mater.* **2018**, *347*, 67–77.
[46] Y. Wang, C. Jiang, Y. Le, B. Cheng, J. Yu, *Chem. Eng. J.* **2019**, *365*, 378–388.
[47] T. D. Nguyen, O. Geuli, L. P. Yeo, S. Magdassi, D. Mandler, A. I. Y. Tok, *Chem. Eur. J.* **2019**, *25*, 16573–16581.
[48] S. Samuei, F. A. Rad, Z. Rezvani, *Appl. Clay Sci.* **2020**, *184*, 105388.
[49] Y. Tian, G. Wang, F. Li, D. G. Evans, *Mater. Lett.* **2007**, *61*, 1662–1666.
[50] Z. M. Ni, S. J. Xia, L. G. Wang, F. F. Xing, G. X. Pan, *J. Colloid Interface Sci.* **2007**, *316*, 284–291.
[51] M. Fathizadeh, H. N. Tien, K. Khivantsev, Z. Song, F. Zhou, M. Yu, *Desalination.* **2019**, *451*, 125–132.
[52] J. Gonçalves, R. Guimaraes, C. Nunes, A. Duarte, B. Brandao, H. Toma, K. Araki, *RSC Adv.* **2016**, *6*, 102504–102512.
[53] A. C. de Sá, L. L. Paim, N. R. Stradiotto, *Int. J. Electrochem. Sci.* **2014**, *9*, 7746–7762.
[54] Y. Zhao, L. Hu, S. Zhao, L. Wu, *Adv. Funct. Mater.* **2016**, *26*, 4085–4093.
[55] W. Liu, H. Niu, J. Yang, K. Cheng, K. Ye, K. Zhu, G. Wang, D. Cao, J. Yan, *Chem. Mater.* **2018**, *30*, 1055–1068.
[56] M. Li, J. Cheng, F. Liu, X. Zhang, *Chem. Phys. Lett.* **2015**, *640*, 5–10.
[57] X. Cao, H.-Y. Zeng, S. Xu, J. Yuan, J. Han, G.-F. Xiao, *Appl. Clay Sci.* **2019**, *168*, 175–183.
[58] H. Gao, Y. Cao, Y. Chen, Z. Liu, M. Guo, S. Ding, J. Tu, J. Qi, *Appl. Surf. Sci.* **2019**, *465*, 929–936.
[59] X. Hua, C.-J. Mao, J.-S. Chen, P.-P. Chen, C.-F. Zhang, *J. Alloys Compd.* **2019**, *777*, 749–758.
[60] K. Le, Z. Wang, F. Wang, Q. Wang, Q. Shao, V. Murugadoss, S. Wu, W. Liu, J. Liu, Q. Gao, *Dalton Trans.* **2019**, *48*, 5193–5202.
[61] J. Li, P. Zhang, X. Zhao, L. Chen, J. Shen, M. Li, B. Ji, L. Song, Y. Wu, D. Liu, *J. Colloid Interface Sci.* **2019**, *549*, 236–245.
[62] A. Tyagi, M. C. Joshi, A. Shah, V. K. Thakur, R. K. Gupta, *ACS Omega.* **2019**, *4*, 3257–3267.
[63] W. Wang, N. Zhang, Z. Ye, Z. Hong, M. Zhi, *Inorg. Chem. Front.* **2019**, *6*, 407–416.
[64] X. Wanga, J. Zhang, S. Yanga, H. Yana, X. Honga, W. Donga, Y. Liu, B. Zhanga, Z. Wen, *Electrochim. Acta.* **2019**, *295*, 1–6.
[65] P.-F. Liu, J.-J. Zhou, G.-C. Li, M.-K. Wu, K. Tao, F.-Y. Yi, W.-N. Zhao, L. Han, *Dalton Trans.* **2017**, *46*, 7388–7391.
[66] K. Fan, H. Chen, Y. Ji, H. Huang, P. M. Claesson, Q. Daniel, B. Philippe, H. Rensmo, F. Li, Y. Luo, L. Sun, *Nat. Commun.* **2016**, *7*, 11981–11989.
[67] Y. Wang, C. Jiang, Y. Le, B. Cheng, J. Yu, *Chem. Eng. J.* **2016**, *45*, 2239–2262.
[68] X.T. Zheng, A. Ananthanarayanan, K. Q. Luo, P. Chen, *Small.* **2015**, *11*, 1620–1636.
[69] Y. Yibo, J. Gong, J. Chen, P. Chen, *Adv. Mater.* **2019**, *31*, 1808283.
[70] A. S. Dezfuli, M. R. Ganjali, H. R. Naderi, P. Norouzi, *RSC Adv.* **2015**, *5*, 46050–46058.
[71] H. R. Naderi, P. Norouzi, M. R. Ganjali, *Physics, Mater. Chem. Phys.* **2015**, *163*, 38–44.
[72] B. Guan, L. Hu, G. Zhang, D. Guo, T. Fu, J. Li, H. Duan, C. Li, Q. Li, *RSC Adv.* **2014**, *4*, 4212–4217.
[73] W. Fu, Y. Wang, W. Han, Z. Zhang, H. Zha, E. Xie, *J. Mater. Chem. A.* **2016**, *4*, 173–182.
[74] J. Zhu, Y. Jiang, Z. Lu, C. Zhao, L. Xie, L. Chen, J. Duan, *J. Colloid Interface Sci.* **2017**, *498*, 351–363.
[75] A. Zolfaghari, H. R. Naderi, H. R. Mortaheb, *J. Electroanal. Chem.* **2013**.
[76] D. Guo, X. Song, L. Tan, H. Ma, W. Sun, H. Pang, L. Zhang, X. Wang, *Chem. Eng. Sci.* **2019**, *356*, 955–963.
[77] Z. Wang, X. Zhang, J. Wang, L. Zou, Z. Liu, Z. Hao, *J. Colloid Interface Sci.* **2013**, *396*, 251–257.
[78] H. Ge, C. Wang, L. Yin, *J. Mater. Chem. A.* **2015**, *3*, 17359–17368.

Manuscript received: September 5, 2020
Revised manuscript received: November 2, 2020
Accepted manuscript online: November 9, 2020